
Article:
Aslam, A., Rehman, A.U., Amin, N. et al. (7 more authors) (2023) To study the structural, electrical, and magnetic properties of M (M = Mg2+, Mn2+, and Cd2+) doped Cu-Ni-Co-La spinel ferrites. Materials Chemistry and Physics, 294. 127034. ISSN 0254-0584

https://doi.org/10.1016/j.matchemphys.2022.127034

To study the structural, electrical, and magnetic properties of *M* (*M* = Mg^{2+}, Mn^{2+}, and Cd^{2+}) doped Cu-Ni-Co-La spinel ferrites

Asma Aslam[a], Atta Ur Rehman[a], M. Amman[b], M. Akhtar[a], N. Amin[a], N. A. Morley[c], Mongi Amami[d,e], Hafiz T Ali[f], Mohammad Yusuf[g], Muhammad Imran Arshad[a]*

[a]*Department of Physics, Government College University, Faisalabad, Pakistan.*
[b]*Department of Mathematics, University of Management and Technology, Lahore 54770, Pakistan.*
[c]*Department of Materials Science and Engineering, The University of Sheffield, UK, S1 3JD.*
[d]*Department of Chemistry College of Sciences, King khalid university, P.O. Box 9004, Abha, Saudi Arabia*
[e]*Laboratoire des Matériaux et de l'environnement pour le développement durable LR18ES10. 9 Avenue Dr. Zoheir SAFI, 1006, Tunis, Tunisia*
[f]*Department of Mechanical Engineering, College of Engineering, Taif University, P.O. Box 1109, Taif 21944, Saudi Arabia*
[g]*Department of Clinical Pharmacy, College of Pharmacy, Taif University, P.O. Box 1109, Taif 21944, Saudi Arabia.*

*Corresponding Author: miarshadgcuf@gmail.com

Abstract

Tertiary $Cu_{0.25}Ni_{0.15}\mathbf{M_{0.25}}Co_{0.35}La_{0.15}Fe_{1.85}O_4$ (**M = Mg^{2+}, Mn^{2+}, and Cd^{2+}**) spinel ferrites powders were prepared using the cost-effective sol-gel auto combustion route. The lattice parameters, absorption and vibrational bands, energy band gap, AC conductivity, and dielectric loss of the as-prepared ferrites were all measured. The Cd^{2+} doped ferrite has a minimum crystallite size (*D*) of 50.9 nm, which is smaller compared to Mg^{2+} and Mn^{2+} doped ferrites. Furthermore, the X-ray diffraction (XRD), as well as Fourier transform infrared radiation (FTIR) and Raman analysis confirmed the doping of Mg^{2+}, Mn^{2+}, and Cd^{2+} ions on their respective lattice sites. The resistivity of the divalent ions (Mg^{2+}, Mn^{2+}, and Cd^{2+}) doped ferrites decreased in the para region and increased in the ferro region as the temperature increased. Moreover, the resistivity of the Cd^{2+} doped ferrite was smaller when compared to the ferrites doped with Mg^{2+} and Mn^{2+} ions. From Arrhenius plots, the minimum activation energy (ΔE) 0.8671 eV was observed for Cd^{2+} doped ferrites. The Cd^{2+} substituted ferrite also has the smallest AC conductivity and dielectric loss compared to Mg^{2+} and Mn^{2+} substituted ferrites. The coercivity and saturation magnetization were 136.41 Oe and 92.29 emu/g for the Cd^{2+} doped ferrite, respectively. These results suggest that the Cd^{2+} doped ferrite material could be used in high-frequency and high-power applications.

Keywords: sol-gel auto combustion; conductivity; activation energies; polaron hopping; high-frequency.

1. Introduction

Magnetic materials such as spinel ferrites (SFs) are important due to their outstanding structural [1], magnetic [2], optical [3], morphological [4], and dielectric [4] properties. At the present, soft ferrite magnetic materials have been used in the industrial, electronics, and biomedical fields for their different applications including microwave absorbing materials [5], target drug delivery [6], magnetoelectric switching [7], magnetic resonance imaging [8], antennas [9], oscillators [10], high sensitive sensors [11], filters [12], magnetic ferrofluids [13], and high-frequency devices [14]. Spinel ferrites are generally expressed by the formula (AB_2O_4) [15] where *A* indicates divalent metal ions including Cu^{2+}, Co^{2+}, Cd^{2+}, $Ni^{2+,}$ Sn^{2+}, etc. and *B* represents trivalent metal cations such as La^{3+}, Ce^{3+}, and Nd^{3+}, etc. Various methods are utilized to prepare SFs including the sol-gel auto combustion (SGAC) route [16], the glass crystallization method [17], the solid-state reaction (SSR) method [18], co-precipitation [19-21], and the microwave method [22]. The SGAC route was found to be better due to its low-temperature preparation, producing better homogeneity of particles, fine surface morphology, and excellent properties [23].

Due to their extraordinary role in different fields, ferrites have gained significant attention from researchers. A small amount of dopant ion within the spinel ferrites is the most appropriate route to modify their structural, dielectric, and electrical characteristics. La^{3+} is the most suitable rare-earth ion for doping because it is a lighter element with high electric and thermal properties compared to the other rare-earth elements [16]. Bharathi *et al*. [24] studied La^{3+} doped cobalt ferrites synthesized through a solid-state chemical reaction. The electric parameters of the La^{3+} doped cobalt ferrites were reduced with a reduction in temperature and the conductivity was 0.623×10^{-8} Ω^{-1} cm^{-1} at room temperature (RT). Kumar *et al*. [25] studied the influence of La^{3+} substitution on $CoFe_2O_4$ spinel ferrite synthesized using a co-precipitation route. The electrical resistivity of prepared pure cobalt ferrite at 300 K was 6.465×10^5 Ω cm, while its value for La^{3+} concentration x = 0.15 was 26.990×10^6 Ω cm. Mulushoa *et al*. [18] prepared Cu-Cr doped Mg^{2+} nano ferrite samples through the SSR process and reported a significant decrease in lattice parameters with the doping of dopant cation. It was also observed that the electrical resistivity increased from 0.553×10^5 to 0.105×10^8 Ω cm due to the substitution of Cu-Cr ions. Hamdaoui *et al*. [26] investigated the properties of Ni-Cd-Mg ferrite synthesized through the sol-gel process, with the lattice parameters increasing with the Cd^{2+} doping increased. The electric conductivity of the prepared samples reveals their semiconductor nature due to the doping of Cd^{2+}. Hossen *et al*. [27] reported the sol-gel method

studied La^{3+} doped Ni-Cu-Cd ferrites and confirmed the formation of spinel ferrites *via* XRD and FTIR analysis. The AC conductivity improved due to the La^{3+} doping. In the current research work, the tertiary $Cu_{0.25}Ni_{0.15}\mathbf{M_{0.25}}Co_{0.35}La_{0.15}Fe_{1.85}O_4$ (**M = Mg^{2+}, Mn^{2+}, and Cd^{2+}**) spinel ferrite powders were prepared *via* the SGAC technique and the structural, absorption, optoelectrical, dielectric, and magnetic analysis are reported.

2. Experimental Part

2.1 Samples preparation

The series of $Cu_{0.25}Ni_{0.15}M_{0.25}Co_{0.35}La_{0.15}Fe_{1.85}O_4$ (M = Mg^{2+}, Mn^{2+}, and Cd^{2+}) SFs were prepared *via* the SGAC route [$Cu_{0.25}Ni_{0.15}\mathbf{Mg_{0.25}}Co_{0.35}La_{0.15}Fe_{1.85}O_4$ (**Mg-CNCL Ferrite**), $Cu_{0.25}Ni_{0.15}\mathbf{Mn_{0.25}}Co_{0.35}La_{0.15}Fe_{1.85}O_4$ (**Mn-CNCL Ferrite**) and $Cu_{0.25}Ni_{0.15}\mathbf{Cd_{0.25}}Co_{0.35}La_{0.15}Fe_{1.85}O_4$ (**Cd-CNCL Ferrite**)]. All the chemicals were purchased from Sigma-Aldrich. The nitrate salts including Cu $(NO_3)_2.3H_2O$ (99.99%), La $(NO_3)_3.6H_2O$ (99.99%), Mn $(NO_3)_2.4H_2O$ (98%), Fe $(NO_3)_3.9H_2O$ (99.95%), Ni $(NO_3)_2.6H_2O$ (97%), Co $(NO_3)_2.6H_2O$ (98%), Mg $(NO_3)_2.6H_2O$ (99%), and Cd $(NO_3)_2.4H_2O$ (98%) were dissolved into distilled water on a magnetic stirrer for the formation of a homogeneous solution according to the stoichiometric measurements. The citric acid (99.5%) was added into distilled water separately, to keep the solution of citric acid and metal nitrate (C/M) solution at 1:1 ratio. The C/M ratio at 1:1 particularly leads to easy igniting and reaction propagation. Higher C/M ratios (2/1, 3/1) can cause slower combustion with the production of a product that was significantly less foamed and more sintered powder, but lower ratios were unable to spark the reaction and required an additional energy source to continue it [28]. Ammonia was added, to obtain a solution with an acquired pH of ~ 7. The heat was turned on at 353 K for the formation of gel and after the gel formation, the temperature of the magnetic stirrer increased up to 473 K, while the gel was converted into ash due to continuous heat. After the formation of ash, grinding was done and the ash was converted into fine powder. The fine powder of the as-prepared ferrites was put into the furnace and sintering was done at 1073 K for 8 h. The flow chart of the SGAC process for the preparation of Mg-CNCL Ferrite, Mn-CNCL Ferrite, and Cd-CNCL Ferrite is depicted in Fig. 1.

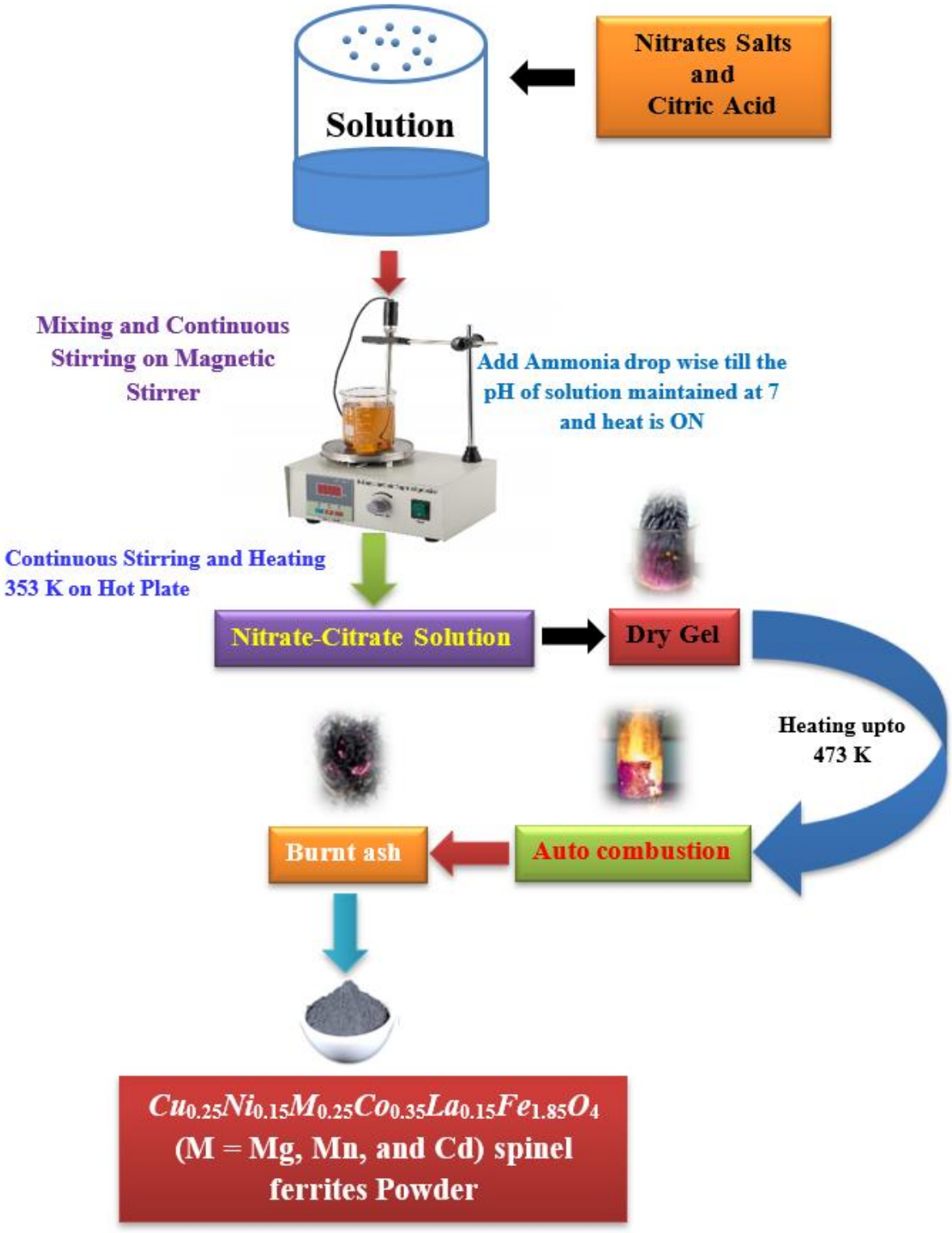

Fig. 1 Flow chart of sol-gel auto combustion technique for the as-prepared ferrites powder

2.2 Characterization Techniques used

Using a Bruker D8 Advance X-ray diffractometer with Cu K_α radiation (λ = 0.1542 nm), X-ray diffraction (XRD) was performed. The FTIR spectrum is used to find the absorption bands. UV-vis spectrum was used to study the optical bandgap energy. The I-V measurements

were taken using Keithley Electrometer Model 2401. Raman spectroscopy was used to study the vibrational characteristics. The dielectric parameters were calculated through an IM3533 LCR Meter. *M-H* loops were measured using a vibrating sample magnetometer (VSM) at RT.

3. Experimental Results and Discussion

3.1 XRD study

Fig.2 indicates the XRD pattern for all the as-prepared sample powders. Diffraction peaks at (220), (311), (222), (400), (422), and (511) confirmed the cubic spinel matrix with space group (*F d -3 m*) for all the prepared samples (JCPDS#75-0541) [16, 29]. The additional peaks confirmed the existence of the orthorhombic secondary phase $LaFeO_3$ (JCPDS#75-0541) in the as-prepared samples having a space group (*P b n m*) [16, 30]. The interplanar distance (*d*) was calculated using Bragg's law, which is given as [31];

$$d = \frac{n\lambda}{2sin\theta} \quad (1)$$

Where n = 1, λ =1.5046 Å, and "θ" indicate Bragg's angle. Equation (2) was employed to determine the experimental lattice constant (*a*) [31];

$$a = d\sqrt{h^2 + k^2 + l^2} \quad (2)$$

where (*hkl*) is the Miller indices. The interplanar distance and experimental lattice constant values are given in Table 1 and have the maximum value for the **Mn-CNCL Ferrite**. The changes in lattice parameters for all the samples is due to the cationic radii difference of the dopant ions, i.e. Mg^{2+} (0.78Å) [26], Mn^{2+} (0.91 Å) [32], Cd^{2+} (1.03 Å) [26], Fe^{3+} ion (0.645 Å) [32] and La^{3+} (1.05 Å) [19]. The crystallite size (*D*) was determined by Scherer's equation [31];

$$D = \frac{0.9\lambda}{\beta Cos\theta} \quad (3)$$

where "β" indicates the full width at half maxima. The values of "*D*" are listed in Table 1. The "*D*" for sample **Mn-CNCL Ferrite** was the largest (58.9 nm) as compared to **Mg-CNCL Ferrite** and **Cd CNCL Ferrite** because of the greater bond energy of Mn-O when compared to the bond energies of Mg-O, Cd-O, La-O, and Fe-O [20].

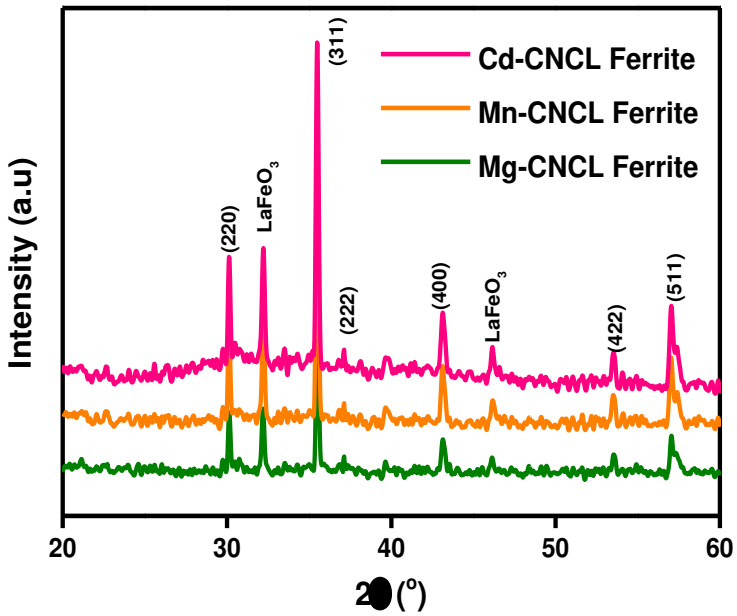

Fig. 2 XRD patterns for as-prepared ferrites

The X-ray (ρ_x) and bulk (ρ_b) densities were determined *via* the relations [31];

$$\rho_x = \frac{8M}{N_A a^3} \quad (4)$$

$$\rho_b = \frac{Mass}{Volume} = \frac{M}{\pi r^2 \times h} \quad (5)$$

where 'r' and 'h' indicate the radius and the thickness of the pellet, respectively. The porosity percentage was determined using equation (6) [31] and is given in Table 1.

$$P\ (\%) = [1 - \frac{\rho_b}{\rho_x}] \times 100 \quad (6)$$

The calculated values of "ρ_x" increased with the insertion of divalent dopant cations while "ρ_b" changed due to the existence of a few certain pores, which arise during the preparation and sintering of the prepared samples [20]. The values of "ρ_x", "ρ_b" and P (%) are reported in Table 1. The strain (ε) [33], specific surface area (S) [33], dislocation density (δ) [33], and packing factor (p) [33] were determined by using formulas from equations (7), (8), (9) and (10) and are given in Table 1.

$$S = \frac{6000}{\rho_x \times D} \quad (7) \qquad p = \frac{D}{d} \quad (8)$$

$$\varepsilon = \frac{1}{d^2} \quad (9) \qquad \delta = \frac{1}{D^2} \quad (10)$$

The surface area, strain, and dislocation density have a minimum value for the **Mn-CNCL Ferrite** but the packing factor (p) was maximum for the **Mn-CNCL Ferrite** (as seen in Table 1). The distance between oxygen ions and tetrahedral (A-) and octahedral (B-) cations are given by the hopping lengths L_A and L_B respectively. A large value of hopping lengths means a higher potential is required to transfer the charge carriers from one lattice site to another while smaller

hopping lengths means a lower potential is needed for the movement of charge carriers into the sublattice [34]. The hopping lengths L_A and L_B were determined *via* the relations (11) and (12) [34];

$$L_A = \frac{a\sqrt{3}}{4} \quad (11)$$

$$L_B = \frac{a\sqrt{2}}{4} \quad (12)$$

The values of "L_A" and "L_B" for all the samples are listed in Table 1. The polaron radius (γ) is calculated using equation (13) [20];

$$\gamma = \frac{1}{2}\sqrt[3]{\frac{\pi a^3}{576}} \quad (13)$$

It was observed that the polaron radius (γ) changed as the experimental lattice constant changed due to the substitution of dopant Mg^{2+}, $Mn^{2+,}$ and Cd^{2+} ions into the as-prepared ferrites.

Table 1 Lattice parameters of the as-prepared samples

Parameters	Mg-CNCL Ferrite	Mn-CNCL Ferrite	Cd-CNCL Ferrite
d (Å)	2.5242	2.5266	2.5241
a (Å)	8.3719	8.3801	8.3715
D (nm)	56.8	58.9	50.9
ρ_x (g/cm^3)	5.4344	5.5818	5.9454
ρ_b (g/cm^3)	3.0569	2.9470	2.9315
P (%)	43.75	52.79	50.69
S (cm^2/g)	0.0194	0.0182	0.0198
p	225.15	233.39	201.71
ε	0.0021	0.0020	0.0023
$\delta \times 10^{-4}$ (nm^{-2})	3.10	2.88	3.86
L_A (Å)	3.6250	3.6286	3.6249
L_B (Å)	2.9595	2.9624	2.9593
γ (Å)	0.7363	0.7375	0.7359

Numerous methods were used by many researchers to find out the distribution of cations [35-37]. The cations distribution is given in Table 2. This arrangement of cations depends on the hypotheses; a) At the *A*- site, the sum cationic arrangement is one, while at the *B*- site, it is two. b) The total charge of the spinel matrix is zero. Therefore, to construct a

neutral structure electrically, the positive and negative charges in the compound are equal. Cadmium ferrite generally has a normal spinel crystal matrix and Cd^{2+} occupies only the *A*-sites [26]. Cobalt and Copper ferrites have partially inverse spinel crystal structures [38] and Co^{2+}, $Cu^{2+,}$ and Fe^{3+} cations occupy both the *A*- and *B*- sites [39]. La^{3+} ions occupy the *B*-site of the lattice [40]. The cationic distribution (Table 2) was used to find out the ionic radii "r_A" and "r_B" to find at *A*- and *B*-sites, respectively for all the as-synthesized ferrites by using equations (14) and (15).

$$r_A = (C_{Cu^{2+}})(r_{Cu^{2+}}) + (C_{Ni^{2+}})(r_{Ni^{2+}}) + (C_{M^{2+}})(r_{M^{2+}}) + (C_{Co^{2+}})(r_{Co^{2+}}) + +(C_{Fe^{3+}})(r_{Fe^{3+}}) \quad (14)$$

$$r_B = \frac{1}{2}[(C_{Cu^{2+}})(r_{Cu^{2+}}) + (C_{Ni^{2+}})(r_{Ni^{2+}}) + (C_{M^{2+}})(r_{M^{2+}}) + (C_{Co^{2+}})(r_{Co^{2+}}) + +(C_{Fe^{3+}})(r_{Fe^{3+}}) + (C_{La^{3+}})(r_{La^{3+}})] \quad (15)$$

where $(C_{Cu^{2+}}), (C_{Ni^{2+}}), (C_{M^{2+}}), (C_{Co^{2+}}), (C_{Fe^{3+}})$ and $(C_{La^{3+}})$ represent the concentration of Cu^{2+}, Ni^{2+}, M^{2+} (Mg^{2+}, Mn^{2+} and Cd^{2+}), Co^{2+}, Fe^{3+} and La^{3+} taken at the *A*-site and *B*-site according to cation distribution while $r_{M^{2+}}$: $r_{Mg^{2+}}$ = tet.:0.57Å and oct.:0.72Å [41]; $r_{Mn^{2+}}$ = tet.:0.655 Å and oct.:0.80 Å [42]; $r_{Cd^{2+}}$ = 1.03 Å [26], $r_{Co^{2+}}$ = tet.:0.58Å and oct.:0.745Å, and $r_{Fe^{3+}}$= tet.: 0.49 Å and oct.: 0.645 Å [43], $r_{Cu^{2+}}$ tet.:0.57Å and oct.:0.73Å [38], $r_{Ni^{2+}}$ = tet.:0.55 Å and oct.:0.69 Å [42], and $r_{La^{3+}}$ = 1.05 Å [44] are the cationic radii of Mg^{2+}, Mn^{2+}, Cd^{2+}, Co^{2+}, Fe^{3+}, Cu^{2+}, Ni^{2+}, and La^{3+} cations, respectively. The calculated ionic radii values for octahedral (r_B) and tetrahedral (r_A) sites are listed in Table 2. The theoretical lattice constant (a_{th}) was determined *via* following equation;

$$a_{th} = \frac{8}{\sqrt[3]{3}}[(r_A + R_o) + 1.73\,(r_B + R_o)] \quad (16)$$

where R_o = 1.32 Å is the ionic radii of oxygen. The values of "a_{th}" are listed in Table 2.

Table 2 Cationic distribution at sub-lattice *A* and *B* sites, tetrahedral and octahedral ionic radii (r_A and r_B), the theoretical lattice constant (a_{th})

Samples	Tetrahedral (*A*) site	Octahedral (*B*) site	r_A (Å)	r_B (Å)	a_{th} (Å)
Mg-CNCL Ferrite	$Cu_{0.0375}Ni_{0.015}Mg_{0.0125}Co_{0.07}Fe_{0.865}$	$Cu_{0.2125}Ni_{0.135}Mg_{0.2375}Co_{0.28}La_{0.15}Fe_{0.985}$	0.5984	0.7157	8.3821
Mn-CNCL Ferrite	$Cu_{0.0375}Ni_{0.015}Mn_{0.2}Co_{0.07}Fe_{0.6775}$	$Cu_{0.2125}Ni_{0.135}Mn_{0.05}Co_{0.28}La_{0.15}Fe_{1.1725}$	0.6108	0.7072	8.3785
Cd-CNCL Ferrite	$Cu_{0.0375}Ni_{0.015}Cd_{0.25}Co_{0.07}Fe_{0.6275}$	$Cu_{0.2125}Ni_{0.135}Co_{0.28}La_{0.15}Fe_{1.2225}$	0.6438	0.7076	8.4304

The tolerance factor (*T*) was estimated by using the following relation (17) [20] and values as seen in Table 3.

$$T = \frac{1}{\sqrt{3}}\left(\frac{r_A + R_O}{r_B + R_O}\right) + \frac{1}{\sqrt{2}}\left(\frac{R_O}{r_A + R_O}\right) \quad (17)$$

The tolerance factor must be close to one for the spinel matrix of soft ferrites [20]. The oxygen positional parameter (*u*) was determined *via* the relation (18) [20];

$$u = (r_A + R_O)\frac{1}{\sqrt{3}a} + \frac{1}{4} \quad (18)$$

It was revealed from Table 3 that the difference in the anion displacement from the ideal structure indicates the small variation of "u" from its ideal value of 0.375 Å due to the synthesis and sintering process [20]. At the A-site (R_A) and B- site (R_B) bond lengths were determined using [33];

$$R_A = (u - 0.25)\left(a\sqrt{3}\right) \quad (19)$$

$$R_B = a\sqrt{\left(3u^2 - \frac{11}{4}u + \frac{43}{64}\right)} \quad (20)$$

The values of "R_A" and "R_B" are listed in Table 3. The shared octahedral edge length (d_{BL}), unshared octahedral edge lengths (d_{BLU}), and tetrahedral edge length (d_{AL}) were estimated using relations [33];

$$d_{BL} = \sqrt{2}\left(2u - \frac{1}{2}\right)a \quad (21)$$

$$d_{BLU} = \left(\sqrt{4u^2 - 3u + \frac{11}{16}}\right)a \quad (22)$$

$$d_{AL} = \sqrt{2}\left(2u - \frac{1}{2}\right)a \quad (23)$$

The bond edge length values are given in Table 3. Inter-ionic lengths are associated with interactions of metal exchange and also reveal the magnetic properties of metal ions. The interionic distance between the ions i.e., Me-O (cation-anion) and Me-Me (cation-cation) interactions are calculated using the following formulas [33];

Me- O interaction (cation-anion):

$$p = \left(\frac{5}{8} - u\right)a \quad (24) \qquad q = \left(U - \frac{1}{4}\right)\sqrt{3}a \quad (25)$$

$$r = \left(u - \frac{1}{4}\right)\sqrt{11}a \quad (26) \qquad s = \left(\frac{1}{3}u + \frac{1}{8}\right)\sqrt{3}a \quad (27)$$

Metal and metal interaction (cation-cation):

$$b = \sqrt{2}\left(\frac{a}{4}\right) \quad (28) \qquad c = \sqrt{11}\left(\frac{a}{8}\right) \quad (29)$$

$$d = \sqrt{3}\left(\frac{a}{4}\right) \quad (30) \qquad e = \sqrt{3}\left(\frac{3a}{8}\right) \quad (31) \qquad f = \sqrt{6}\left(\frac{a}{4}\right) \quad (32)$$

The calculated values of Me-O (p-s) and Me-Me (b-f) are reported in Table 4. The variation in the calculated values of inter-ionic distance between metal ions observed due to doping of divalent Mg^{2+}, Mn^{2+}, and Cd^{2+} ions and interionic distance used to determine the θ_1, θ_2, θ_3, θ_4, and θ_5 bond angles using equations [45];

$$\theta_1 = \left(\frac{p^2+q^2-c^2}{2pq}\right) \quad (33) \qquad \theta_2 = \left(\frac{p^2+r^2-e^2}{2pr}\right) \quad (34)$$

$$\theta_3 = \left(\frac{2p^2 - b^2}{2p^2}\right) \quad (35) \qquad \theta_4 = \left(\frac{p^2 + s^2 - f^2}{2ps}\right) \quad (36)$$

$$\theta_5 = \left(\frac{r^2 + q^2 - d^2}{2rq}\right) \quad (37)$$

The bond angles values are reported in Table 4 and the pictorial representation of *A*–*B*, *A*–*A*, and *B*–*B* interactions with the bond angles are depicted in Fig. 3.

Table 3 Tolerance factor (*T*), oxygen position parameter (*u*), bond lengths (R_A, R_B), Bond edge lengths (d_{AL}, d_{BL}, and d_{BLU}) for all the as-synthesized ferrites

Samples	Tolerance factor	Oxygen position parameter	Bond lengths (Å)		Bond edge lengths (Å)		
	T	***U***	R_A	R_B	d_{AL}	d_{BL}	d_{BLU}
Mg-CNCL Ferrite	1.0306	0.38214	1.9161	2.0332	3.1289	2.7909	2.9623
Mn-CNCL Ferrite	1.0333	0.38305	1.9312	2.0276	3.1536	2.7721	2.9658
Cd-CNCL Ferrite	1.0345	0.38449	1.9501	2.0134	3.1845	2.7351	2.9640

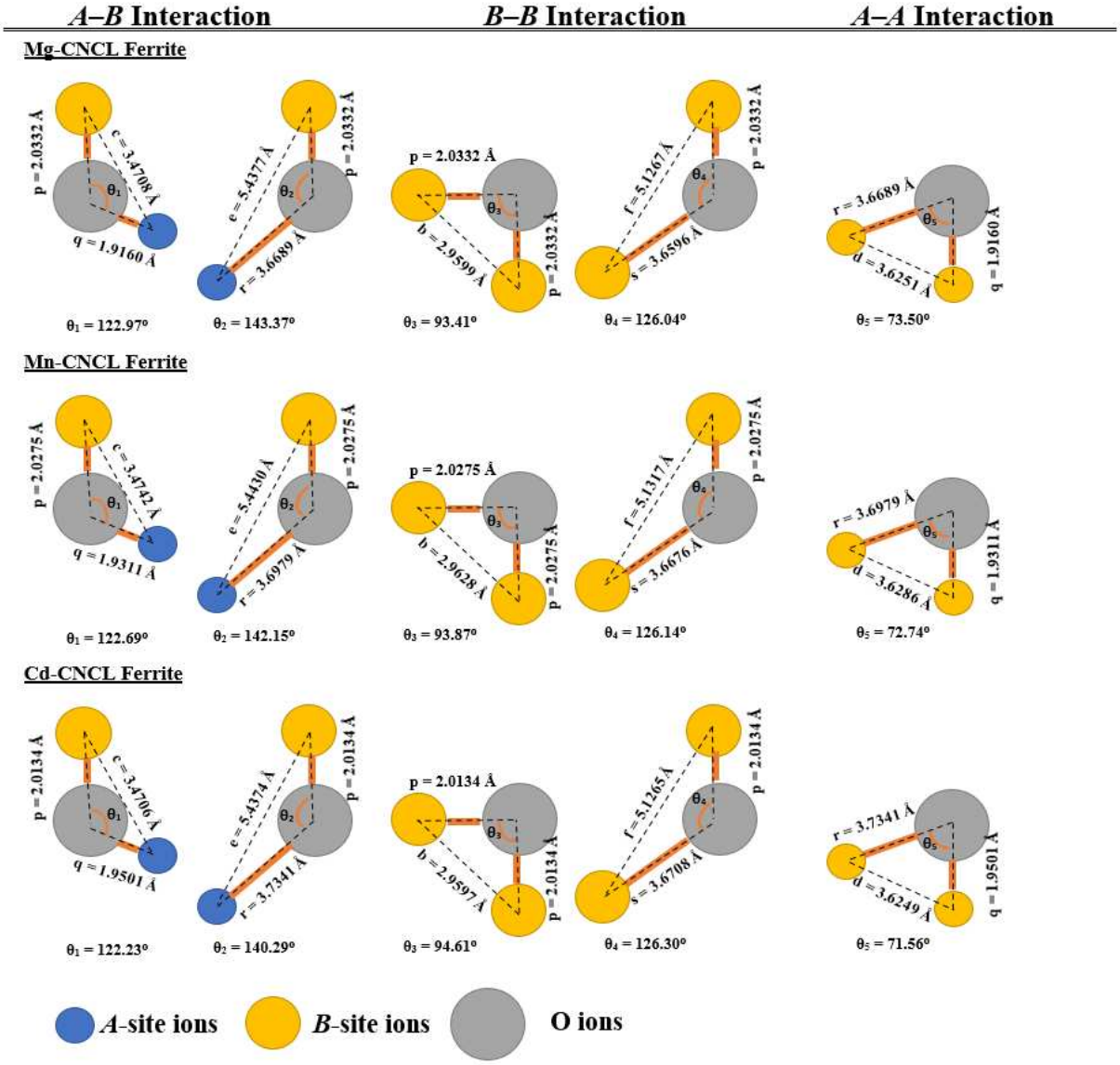

Fig. 3 *A–B*, *B–B*, and *A–A* interactions along with bond angles

Table 4 The bond lengths between Me-O (cation-anion), Me-Me (cation-cation) interactions, and bond angles

Parameters		Mg-CNCL Ferrite	Mn-CNCL Ferrite	Cd-CNCL Ferrite
Cation–Anion (Me –O) Bond length	p (Å)	2.0332	2.0275	2.0134
	q (Å)	1.9160	1.9311	1.9501
	r (Å)	3.6689	3.6979	3.7341
	s (Å)	3.6596	3.6676	3.6708
Cation–Cation (Me –Me) Bond length	b (Å)	2.9599	2.9628	2.9597
	c (Å)	3.4708	3.4742	3.4706
	d (Å)	3.6251	3.6286	3.6249
	e (Å)	5.4377	5.4430	5.4374
	f (Å)	5.1267	5.1317	5.1265
Bond length Angles	θ_1	122.97	122.69	122.23
	θ_2	143.37	142.15	140.29
	θ_3	93.41	93.87	94.61
	θ_4	126.04	126.14	126.30
	θ_5	73.50	72.74	71.56

3.2 Absorption bands analysis

FTIR spectroscopy is a spectroscopic technique that uses the existence of various absorption bands in the lattice sites to gain information about the location of ions within the lattice sites as well as cation distribution [20]. FTIR spectra in the range of 400-4000 cm^{-1} for the as-prepared ferrites are given in Fig. 4(a). The zoom view of FTIR spectra for all the as-prepared samples is given in Fig. 4(b-c) in the range of 400-800 cm^{-1}. The two major absorption bands were found i.e., the high-frequency band (v_T) at the tetrahedral (*A*-) site around 500-600 cm^{-1} (Table 5) while the low frequency band (v_O) at the octahedral (*B*-) site 400-500 cm^{-1} (Table 5). The peaks around 2361 cm^{-1} are from ambient CO_2 gas [20]. The force constants (*K*) were determined *via* the following relation [31];

$$K = 4\pi^2 v^2 c^2 m \tag{38}$$

where m, c, and v represent the reduced mass, speed of light, and wavenumber, respectively. The force constant changed with the addition of the divalent cations Mg^{2+}, Mn^{2+}, and Cd^{2+} at octahedral (K_O) and tetrahedral (K_T) sites are given in Table 5.

Table 5 FTIR parameters of the as-synthesized samples

Samples	v_T	v_O	K_T	K_O
	(cm^{-1})		× 10^5 (dyne/cm^{-1})	
Mg-CNCL Ferrite	575.2	428.5	3.0576	1.6968
Mn-CNCL Ferrite	579.4	420.3	3.1024	1.6325
Cd-CNCL Ferrite	588.7	417.8	3.2028	1.6131

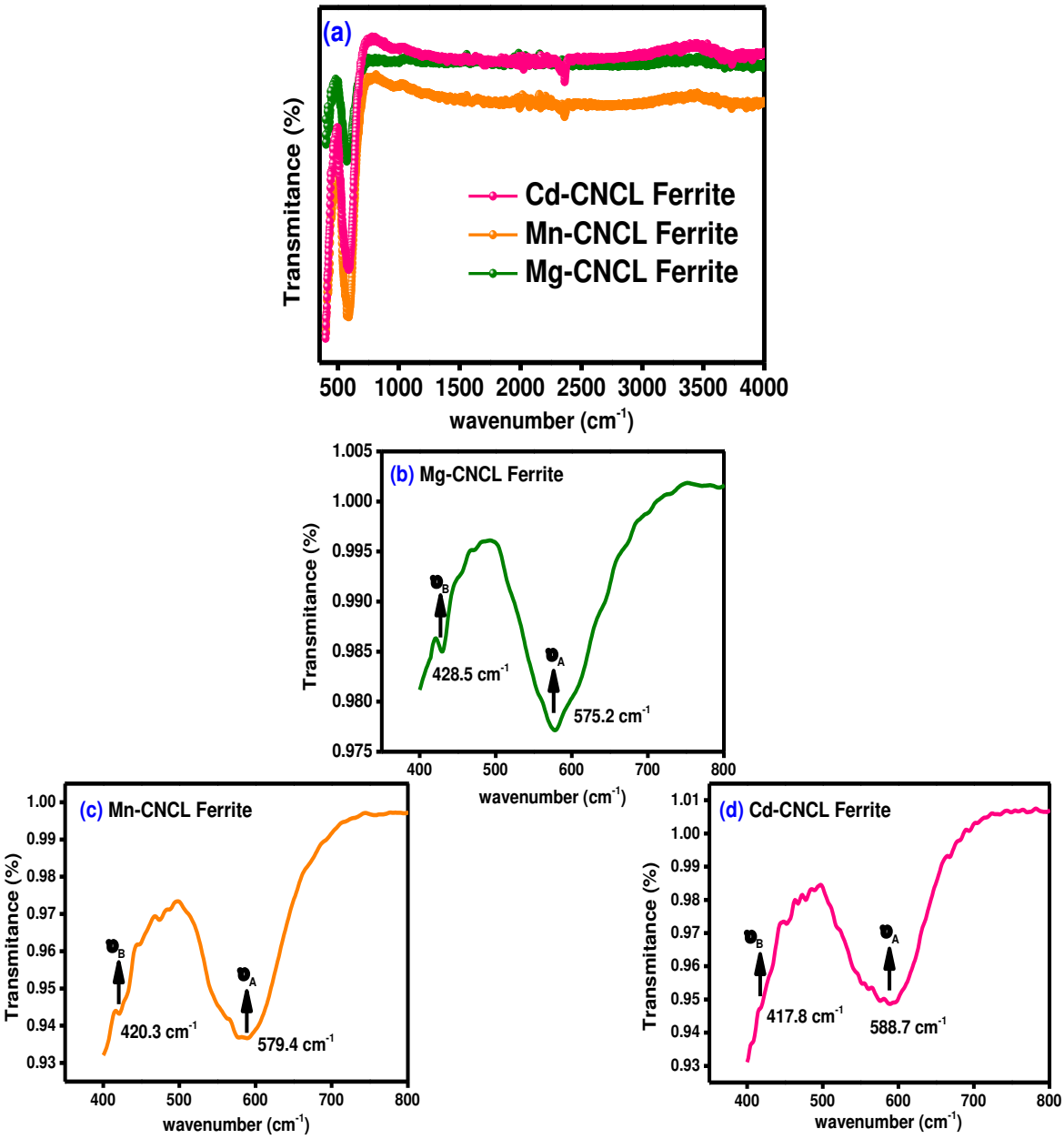

Fig. 4(a) Combine FTIR spectra **(b-d)** Zoom view of FTIR spectra for the as-prepared samples

3.3 Vibrational bands analysis

Raman spectra as shown in Fig. 5 in the range of 150-800 cm^{-1} were recorded and used to investigate the vibrational bands and also structural characteristics associated with the as-synthesized ferrite samples. Fig. 5 revealed the most prominent peaks of Raman modes E_g, T_{2g} (3), and A_{1g} (2) of all the samples, and their values are reported in Table 6.

The symmetric stretching of the oxygen ion is linked with the A_{1g} mode, the symmetric bending of the oxygen anion is due to the E_g mode, and the asymmetric stretching of the oxygen ion is attributed to the T_{2g} mode with respect to the *A*- and *B*- sites cations [20]. It was observed

that in Fig. 5 and Table 6 the as-synthesized ferrites have Raman modes at ~195 cm^{-1}, ~320 cm^{-1}, ~475 cm^{-1}, ~558 cm^{-1}, ~609 cm^{-1}, ~687 cm^{-1}. At around 687 cm^{-1}, Raman modes at the lower wavenumber side (~609 cm^{-1}) revealed a shoulder-like peak. At the tetrahedral site, the stretching vibrations of the Fe–O, and M–O bonds were demonstrated by the A_{1g} (1) and A_{1g} (2) modes [46, 47]. At the *B*- site, E_g and T_{2g} (3) was due to asymmetric, and symmetric bending of oxygen [46, 47] relative to Fe seemed at ~320 cm^{-1} and ~558 cm^{-1}, respectively. Asymmetric stretching of the Fe-O bond also at the *B*- site is represented by T_{2g} (2) [46, 47] and observed at ~475 cm^{-1}. The T_{2g} (1) mode corresponds to tetrahedron translational motion (Fe-O_4) [46, 47] and is present at ~195 cm^{-1}.

Table 6 Raman modes of as-synthesized ferrite samples

Samples	T_{2g} (1)	E_g	T_{2g} (2)	T_{2g} (3)	A_{1g} (2)	A_{1g} (1)
	Tetrahedral site	Octahedral site			Tetrahedral site	
	cm^{-1}					
Mg-CNCL Ferrite	195	320	475	558	609	687
Mn-CNCL Ferrite	197	324	464	559	618	686
Cd-CNCL Ferrite	199	325	463	560	619	685

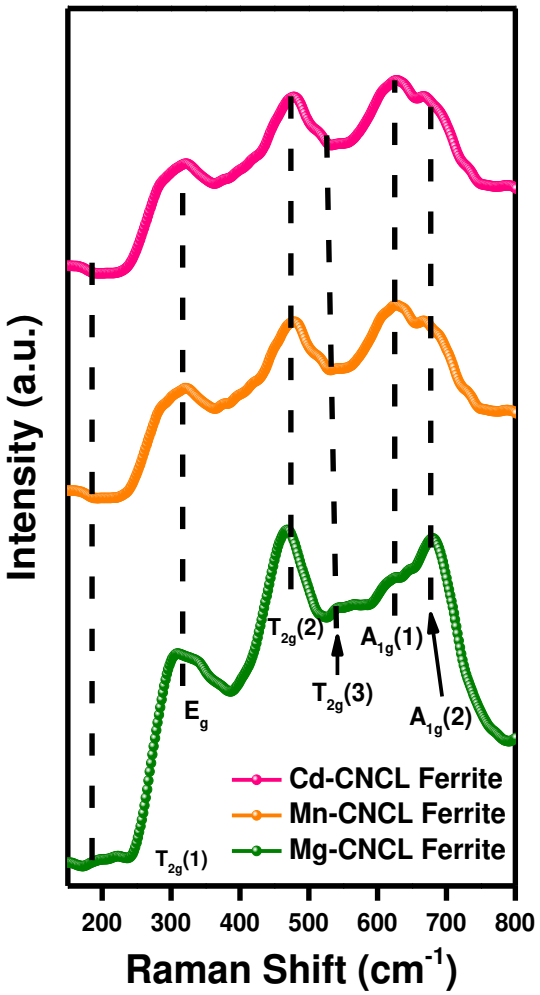

Fig. 5 Raman spectra of the as-prepared ferrites

3.4 Optical bandgap energy analysis

The optical bandgap energy (E_g) was studied using UV-vis spectroscopy for the as-synthesized ferrite samples. Equation (39) is used to calculate the coefficient of absorption given as [48];

$$\alpha = 2.303 \frac{log log\, A}{t} \qquad (39)$$

where "A" is the absorbance and "t" indicates the length in which the sample was placed. Tauc's relation was utilized to determine "E_g" which is given as [48];

$$\alpha hv = B(hv - E_g)^m \qquad (40)$$

where, "m" is a constant which is 2 and ½ for an indirect and direct bandgap of the samples, respectively. Fig. 6(a-c) shows the plots of "hv" *versus* $(\alpha hv)^2$ used to calculate "E_g" of the as-synthesized samples. The calculated optical bandgap energy (E_g) for all the samples is given

in Fig. 6(a-c) and the maximum value was 1.95 eV for the Cd-CNCL Ferrite. The as-prepared samples optical bandgap energy suggest that the materials are a good candidate for optical applications including visible light absorption application.

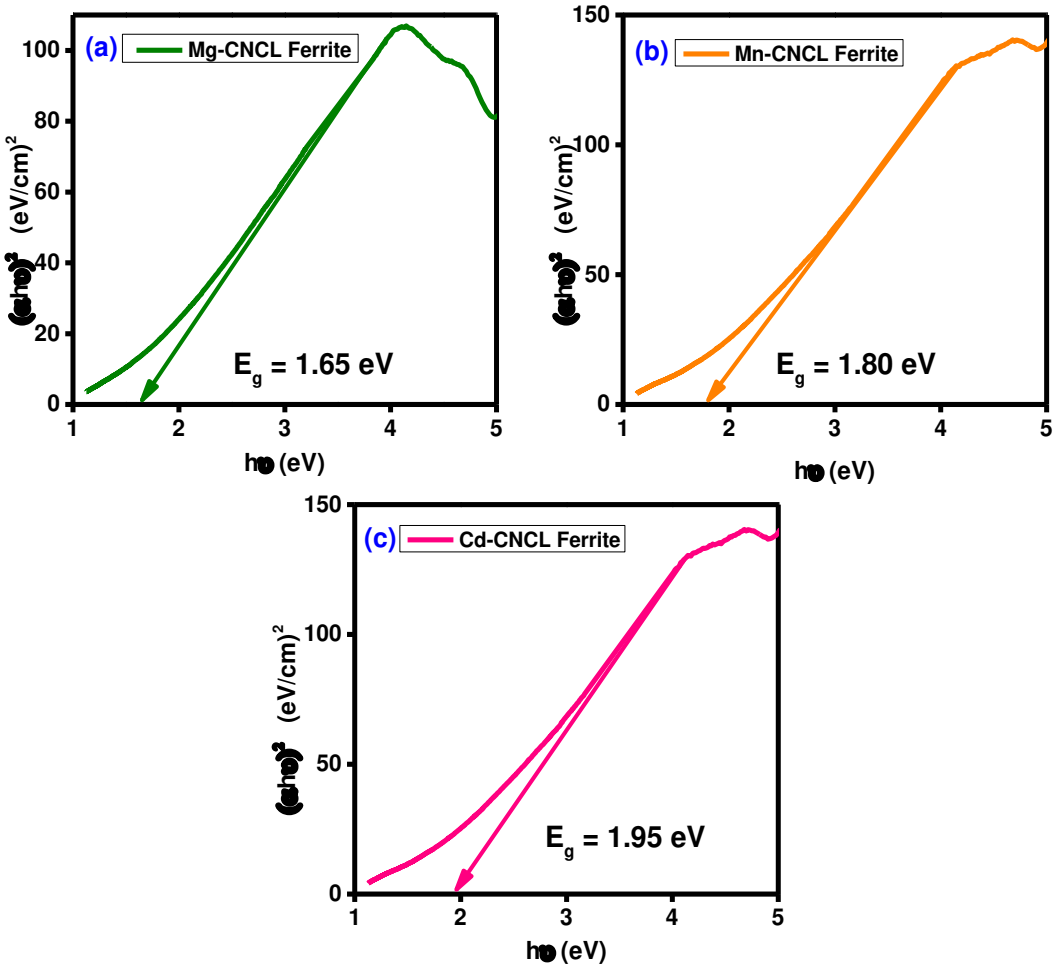

Fig. 6(a-c) Tauc's plots for the as-prepared samples

3.5 I-V Characterization analysis

The electrical properties of the spinel ferrites were altered by the partial replacement of Fe^{3+} with divalent and trivalent cations, which caused lattice distortion and strain. The electrical resistivity (ρ) depends on the synthesized process and composition which varies with the distribution of cations at the *A*- and *B*- sites [16]. The electrical resistivity of the as-prepared samples was determined *via* the following relation [49];

$$\rho = \frac{RA}{L} \qquad (41)$$

where, L = thickness of pellet, A = Area of the pellet. Fig 7 shows the Arrhenius plots of the as-prepared samples. The activation energy (ΔE) was estimated by taking the slope of Arrhenius plots using the following relation [49];

$$\Delta E = 2.303 \times k_B \times 1000 \times slope\ (eV) \quad (42)$$

where k_B represents Boltzmann constant. The Curie temperature (T_C) is the temperature at which a material transitions from one state of electrical resistivity to another state (as seen in Fig 7). At "T_C" magnetic disorder occurs within the as-prepared ferrites. Also, the ferrite's material behavior changes from ferromagnetic to paramagnetic. The region below the "T_C" is known as the ferro region and above the "T_C" is known as the para region. The calculated values of activation energy for the as-synthesized ferrites are given in Fig 8.

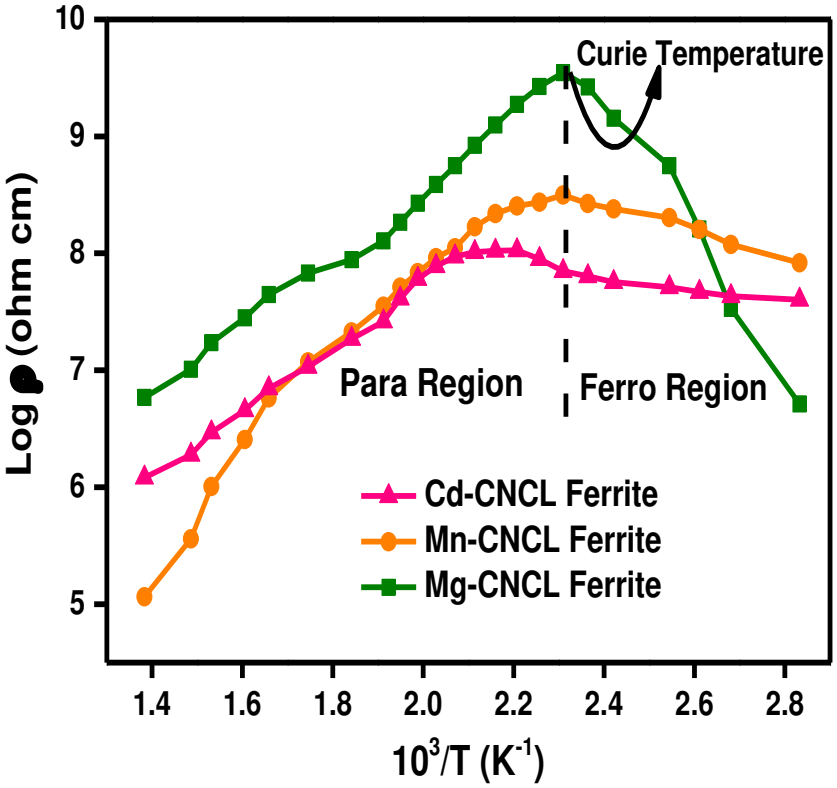

Fig. 7 Graph between 10^3/T and log of resistivity

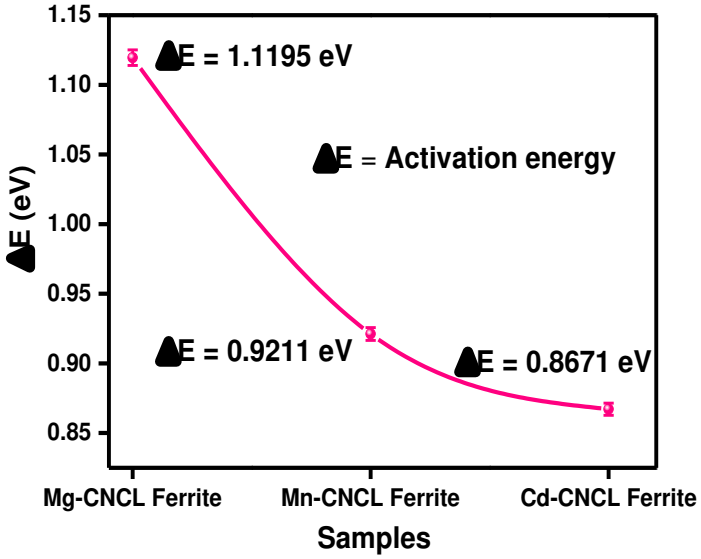

Fig. 8 Activation energy for all the samples

The electrical resistivity was decreased as the temperature in the para region increased as represented in Fig 9(a-b). The maximum electrical resistivity was observed for the Mg-CNCL Ferrite. The change in electrical resistivity may be due to charge hopping caused by different conducting channels including Fe^{3+}–Fe^{3+} and Fe^{3+}–Me (Me is Cd^{2+}, Cu^{2+}, Co^{2+}, Ni^{2+}, Mn^{2+}, and La^{3+}) [16]. The high resistivity suggests that the ferrites are useful for computer memories, electrical and electronic devices, high-density information storage, high-quality filters, high-frequency transformers, magnetic recording media, magnetic resonance imaging, magnetic sensors, microwave absorption, multi-layered chip inductors, power applications, radio frequency circuits, transformer cores, microwave devices, and many more [50].

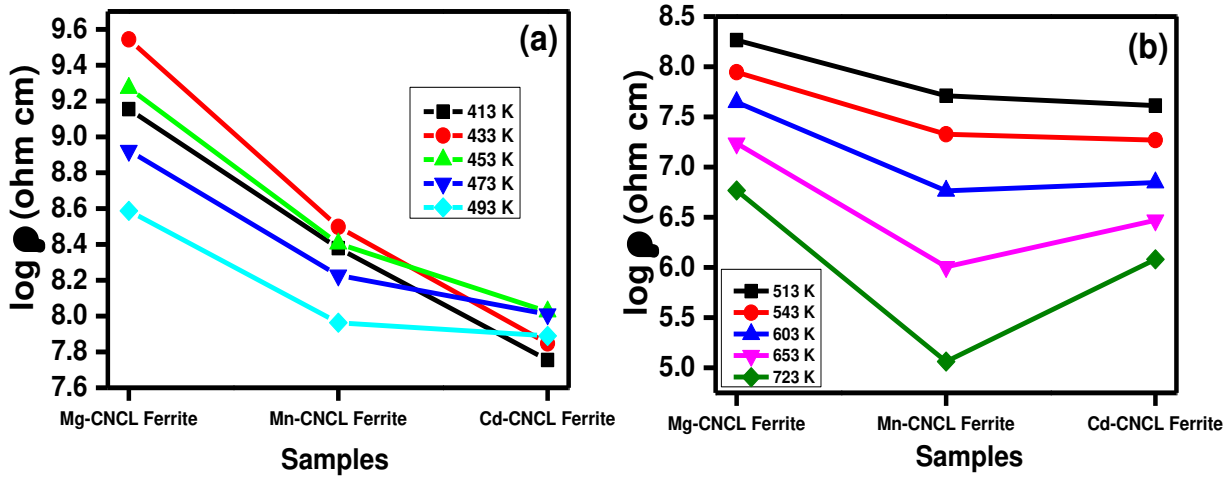

Fig. 9(a) Electrical resistivity in ferromagnetic region **(b)** Electrical resistivity in paramagnetic region

3.6 Dielectric analysis:

The particle composition, distribution of cations, preparation technique, temperature of sintering, and the ratio between Fe^{2+} and Fe^{3+} can change the dielectric characteristics of the ferrites [51]. The low value of the dielectric tangent loss for they could be used in microwave applications [52]. The dielectric tangent loss is reduced with rising frequency and at a certain frequency limit, the dielectric tangent loss (tanδ) becomes almost constant (as depicted in Fig. 10(a)). In the presence of an applied AC field, dielectric tangent loss (tanδ) is the electrical energy lost in the form of heat. At lower frequencies (Fig. 10(b)) the tanδ is higher because at lower frequency values there is a high resistivity in the polarization process. At high frequencies (Fig. 10(c)) the resistivity magnitudes are low in the polarization process, therefore the dielectric tangent loss values were small. So, in the present study, it is noted that for the sample CD the dielectric tangent loss was a minimum. The AC conductivity (σ) was determined by using equation [53];

$$\sigma = 2\pi f tan\delta \tag{43}$$

Fig. 11 revealed that the log of frequency *versus* the AC conductivity (σ) and minimum AC conductivity (σ) was observed for the CD sample. The values of "σ" were increased as the frequency increased due to the low conductivity of the grain boundaries. This change in AC conductivity (σ) is due to grain boundaries possessing low conductivity and the grains are highly conductive which is well-matched with Koop's theory of polarization [53].

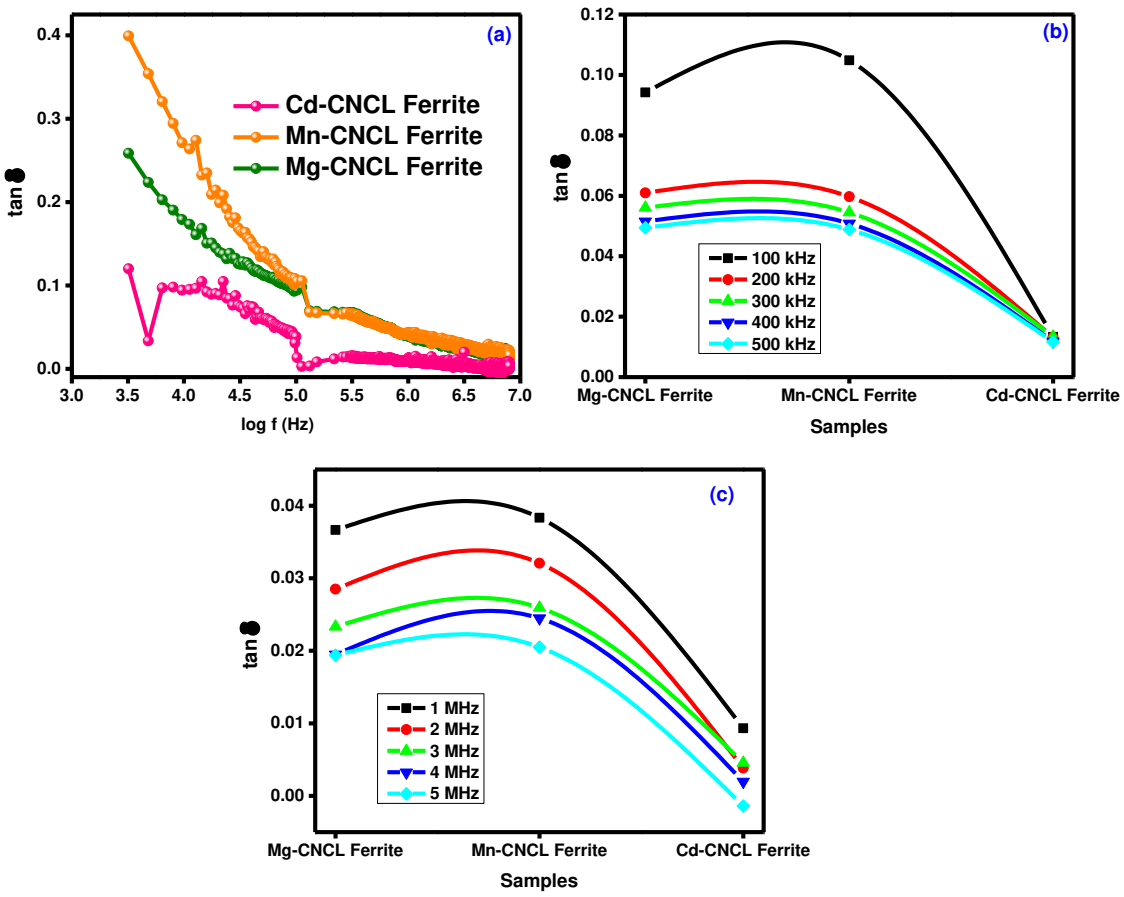

Fig. 10(a) Log of frequency *versus* dielectric tangent loss **(b-c)** dielectric tangent loss at different frequencies

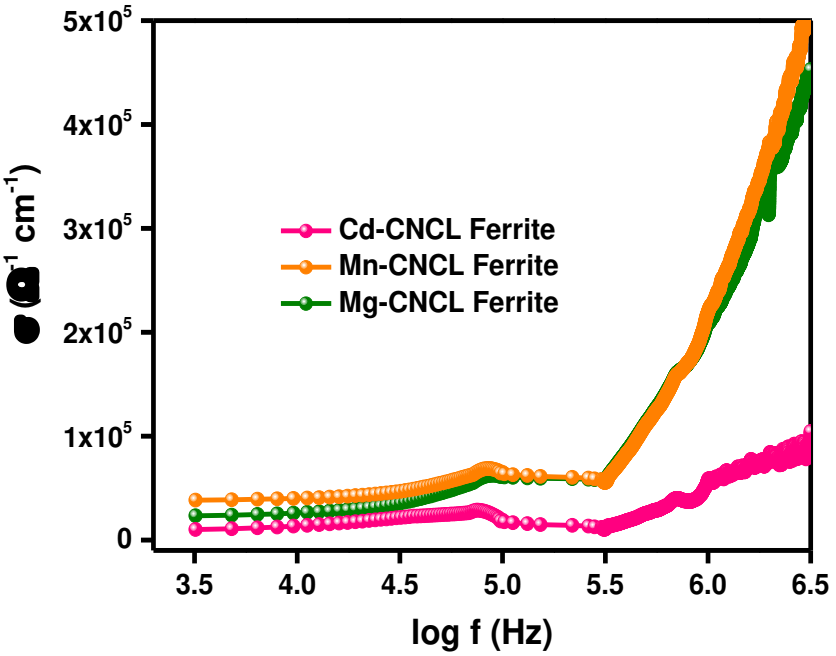

Fig. 11 log of frequency *versus* AC conductivity of the as-prepared samples

3.7 Magnetic properties

Data storage, magnetization switching devices, spintronic devices, and functional materials could all benefit from the magnetic performance of conventional spinel ferrites [54]. The **Mg-CNCL**, **Mn-CNCL**, and **Cd-CNCL** sample's *M-H* loops are depicted in Fig. 12(a), while Fig. 12(b) gives the applied field *versus* microwave frequency (ω_m) plots for all the samples. The S-shaped hysteresis loops were seen in all samples, which are typical loops for soft magnetic materials, indicating that the material has soft ferromagnetic properties. The anisotropic density, *A–B* interactions, and grain growth are all factors that influence magnetic parameters [55]. The magnetic characteristics of CNCL ferrite are considerably influenced by the addition of Mg^{2+}, Mn^{2+}, and Cd^{2+} ions. The remanence (M_r), coercivity (H_C), saturation (M_s) magnetization, anisotropy constant (K), squareness ratio (SQ), initial permeability (μ_i), and microwave frequency (ω_m) of all the samples are seen in Table 7. The minimum remanence and maximum saturation magnetization were observed for the Mn-CNCL sample (as seen in Table 7) and the squareness ratio was also minimum for the Mn-CNCL sample (as seen in Table 7). The variation in saturation magnetization may be due to different magnetic moment of the divalent ion such as Mg^{2+} (0 μ_B) [56], Mn^{2+} (4.5 μ_B) [57], and Cd^{2+} (0 μ_B) [56]. The reduction in coerciveness (as seen in Table 7) with the addition of divalent ions (Mg^{2+}, Mn^{2+}, and Cd^{2+}) was due to a reduction in anisotropic fields, which reduced the domain wall energy coercive. The small coercivity indicates that the as-synthesized ferrites can be easily demagnetized for electromagnetic applications. The anisotropy constant ($K = \frac{H_c \times M_s}{0.96}$) [33], and initial permeability ($\mu_i = \frac{M_s^2 \times D}{K}$) [33] were determined and both showed an opposite trend with the doping of Mg^{2+}, Mn^{2+}, and Cd^{2+} ions as reported in Table 7. The microwave frequency ($\omega_m = 8\pi^2 M_s \gamma$) was calculated [16, 48, 58-60], where gyromagnetic fraction (γ) is 2.8 MHz/Oe. The microwave frequency is proportional to the saturation magnetization, and the smaller the microwave frequency means the saturation magnetization is small. The microwave frequency was maximum for the Mn-CNCL sample.

Table 7 Magnetic parameters of all the as-prepared samples

Samples	H_C (Oe)	SQ	M_r (emu/g)	M_s (emu/g)	K (erg/cm^3)	μ_i	ω_m (GHz)
Mg-CNCL Ferrite	470.81	0.449	38.79	86.24	42294.43	9.98	19.06
Mn-CNCL Ferrite	214.69	0.335	35.62	106.29	23770.20	27.99	23.49
Cd-CNCL Ferrite	136.41	0.395	36.52	92.29	13113.83	33.05	20.40

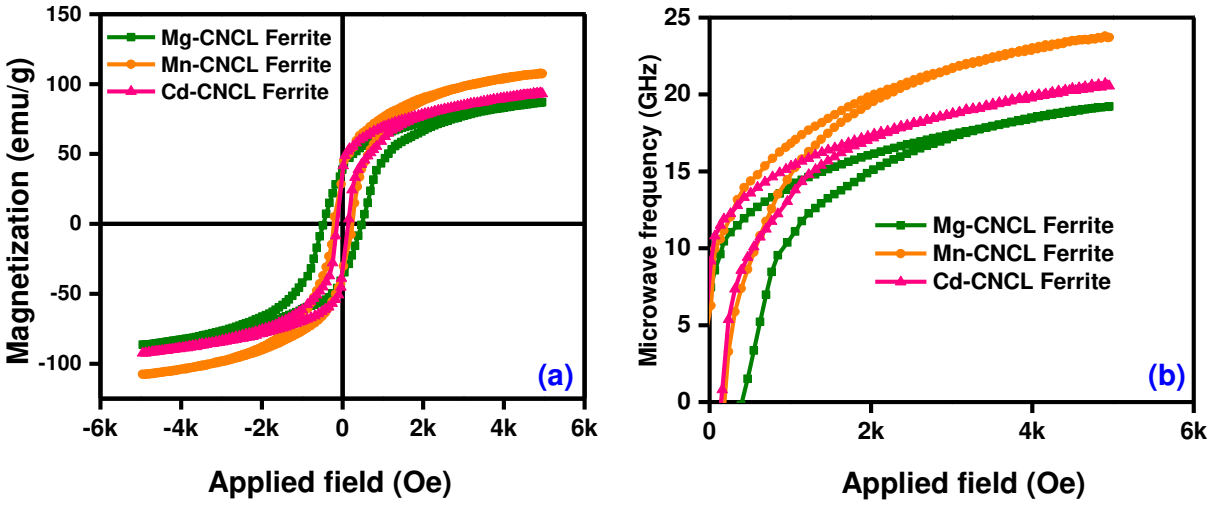

Fig. 12(a) Hysteresis (*M-H*) loops **(b)** Applied field *versus* microwave frequency of the as-prepared samples

Conclusions

In this present study, we report on the investigation of the structural, absorption, vibrational, optoelectrical, and dielectric properties of $Cu_{0.25}Ni_{0.15}\boldsymbol{M_{0.25}}Co_{0.35}La_{0.15}Fe_{1.85}O_4$ (**M= Mg^{2+}, Mn^{2+}, and Cd^{2+}**) ferrites prepared using SGAC process. The smallest crystallite size was observed for Cd^{2+} ferrite compared with the Mg^{2+} and Mn^{2+} doped ferrites. The lattice parameters variation was determined from XRD, and absorption bands from FTIR and Raman modes at the *A*- and *B*- sites confirmed the substitution divalent (Mg^{2+}, Mn^{2+}, and Cd^{2+}) cations at the lattice sites. The maximum optical bandgap energy was 1.95 eV for Cd^{2+} substituted CNCL ferrite when compared with Mg^{2+} and Mn^{2+} substituted CNCL ferrites. The resistivity was increased in the ferromagnetic region and reduced in the paramagnetic region as the temperature was increased. Furthermore, the minimum activation energy was 0.8671 eV for Cd^{2+} doped CNCL ferrite. The AC conductivities of the as-prepared ferrites increase as the frequency rises and minimum dielectric loss was found for Cd^{2+} doped CNCL ferrite compared with substituted Mg^{2+} and Mn^{2+} ions in CNCL ferrites. The smallest coercivity was observed and the microwave frequency was 20.40 GHz for Cd^{2+} doped CNCL ferrite. Therefore, the increase in conductivity may be linked to an increase in charge carrier thermally activated drift mobility and our finding suggests that such a promising function of Cd^{2+} doped CNCL ferrite, means it could be used in high-frequency and high-power applications.

Authorship contribution statement

Asma Aslam: Writing – original draft, **Atta Ur Rehman:** Conceptualization, Investigation, **M. Amman:** Validation, **Maria Akhtar:** Methodology, **Nasir Amin:** Visualization, **N.A. Morley:** Writing – review & editing, **Mongi Amami:** Resources, **Hafiz T Ali:** Formal analysis

& Resources, **Mohammad Yusuf:** Resources & Data curation, **Muhammad Imran Arshad:** Conceptualization, Supervision.

References

[1] K. Hussain, N. Amin, M.I. Arshad, Evaluation of structural, optical, dielectric, electrical, and magnetic properties of Ce^{3+} doped $Cu_{0.5}Cd_{0.25}Co_{0.25}Fe_{2-x}O_4$ spinel nano-ferrites, Ceramics International, 47 (2021) 3401-3410.

[2] R.S. Yadav, J. Havlica, J. Masilko, L. Kalina, J. Wasserbauer, M. Hajdúchová, V. Enev, I. Kuřitka, Z. Kožáková, Impact of Nd^{3+} in $CoFe_2O4$ spinel ferrite nanoparticles on cation distribution, structural and magnetic properties, Journal of Magnetism and Magnetic materials, 399 (2016) 109-117.

[3] C. Kumari, H.K. Dubey, F. Naaz, P. Lahiri, Structural and optical properties of nanosized Co substituted Ni ferrites by coprecipitation method, Phase Transitions, (2020) 1-10.

[4] T. Tatarchuk, I. Mironyuk, V. Kotsyubynsky, A. Shyichuk, M. Myslin, V. Boychuk, Structure, morphology and adsorption properties of titania shell immobilized onto cobalt ferrite nanoparticle core, Journal of Molecular Liquids, 297 (2020) 111757.

[5] A.R. Bueno, M.L. Gregori, M.C. Nóbrega, Microwave-absorbing properties of $Ni_{0.50-x}Zn_{0.50-x}Me_{2x}Fe_2O_4$ (Me = Cu, Mn, Mg) ferrite–wax composite in X-band frequencies, Journal of Magnetism and Magnetic Materials, 320 (2008) 864-870.

[6] N. Sulaiman, M.J. Ghazali, B.Y. Majlis, J. Yunas, M. Razali, Superparamagnetic calcium ferrite nanoparticles synthesized using a simple sol-gel method for targeted drug delivery, Bio-medical materials and engineering, 26 (2015) S103-S110.

[7] M. Bichurin, R. Petrov, Y.V. Kiliba, Magnetoelectric microwave phase shifters, Ferroelectrics, 204 (1997) 311-319.

[8] Z. Ghasemian, D. Shahbazi-Gahrouei, S. Manouchehri, Cobalt zinc ferrite nanoparticles as a potential magnetic resonance imaging agent: An in vitro study, Avicenna journal of medical biotechnology, 7 (2015) 64.

[9] F. Reggia, E. Spencer, A new technique in ferrite phase shifting for beam scanning of microwave antennas, Proceedings of the IRE, 45 (1957) 1510-1517.

[10] M.T. Weiss, A solid-state microwave amplifier and oscillator using ferrites, Physical Review, 107 (1957) 317.

[11] J. Paulsen, A. Ring, C. Lo, J.E. Snyder, D.C. Jiles, Manganese-substituted cobalt ferrite magnetostrictive materials for magnetic stress sensor applications, Journal of Applied Physics, 97 (2005) 044502.

[12] H. Tanbakuchi, D. Nicholson, B. Kunz, W. Ishak, Magnetically tunable oscillators and filters, IEEE Transactions on Magnetics, 25 (1989) 3248-3253.

[13] I. Sharifi, H. Shokrollahi, S. Amiri, Ferrite-based magnetic nanofluids used in hyperthermia applications, Journal of Magnetism and Magnetic Materials, 324 (2012) 903-915.

[14] N. Hiratsuka, Soft magnetic hexagonal ferrites for high frequency devices, Journal of the Magnetics Society of Japan, 37 (2013) 141-146.

[15] N.M. Astik, P.K. Jha, Investigation of structural and electrical properties of mixed ferrite system, in: AIP Conference Proceedings, AIP Publishing LLC, 2015, pp. 070001.

[16] A.U. Rehman, N. Morley, N. Amin, M.I. Arshad, M.A. un Nabi, K. Mahmood, A. Ali, A. Aslam, A. Bibi, M.Z. Iqbal, Controllable synthesis of La^{3+} doped $Zn_{0.5}Co_{0.25}Cu_{0.25}Fe_{2-x}La_xO_4$ (x = 0.0, 0.0125, 0.025, 0.0375, 0.05) nano-ferrites by sol-gel auto-combustion route, Ceramics International, 46 (2020) 29297-29308.

[17] S. Woltz, R. Hiergeist, P. Görnert, C. Rüssel, Magnetite nanoparticles prepared by the glass crystallization method and their physical properties, Journal of Magnetism and Magnetic Materials, 298 (2006) 7-13.
[18] S.Y. Mulushoa, N. Murali, M.T. Wegayehu, S. Margarette, K. Samatha, Influence of Cu-Cr substitution on structural, morphological, electrical and magnetic properties of magnesium ferrite, Results in physics, 8 (2018) 772-779.
[19] I. ALIa, N. Amin, A. REHMAN, M. Akhtar, M. Fatima, K. Mahmood, A. ALIa, G. Mustafa, M. Hasan, A. Bibi, ELECTRICAL AND MAGNETIC PROPERTIES OF $BaCo_xCd_{2-x}Fe_{16}O_{27}$ W-TYPE HEXAFERRITES ($0\leq x\leq 0.5$), Digest Journal of Nanomaterials Biostructures, 15 (2020), 67-73.
[20] A. Aslam, A.U. Rehman, N. Amin, M.A. un Nabi, Q. ul ain Abdullah, N. Morley, M.I. Arshad, H.T. Ali, M. Yusuf, Z. Latif, Lanthanum doped $Zn_{0.5}Co_{0.5}La_xFe_{2-x}O_4$ spinel ferrites synthesized via co-precipitation route to evaluate structural, vibrational, electrical, optical, dielectric, and thermoelectric properties, Journal of Physics and Chemistry of Solids, 154 (2021) 110080.
[21] N. Amin, M. Akhtar, M. Sabir, K. Mahmood, A. ALIa, G. Mustafa, M. Hasan, A. Bibi, M. Iqbal, F. Iqbal, SYNTHESIS, STRUCTURAL AND OPTICAL PROPERTIES OF Zn-SUBSTITUTED Co W-FERRITES BY COPRECIPITATION METHOD, Journal of Ovonic Research, 16 (2020) 11-19.
[22] R. Melo, F. Silva, K. Moura, A. De Menezes, F. Sinfrônio, Magnetic ferrites synthesised using the microwave-hydrothermal method, Journal of Magnetism and Magnetic Materials, 381 (2015) 109-115.
[23] M.N. Akhtar, A.B. Sulong, M. Akhtar, M.A. Khan, Systematic study of Ce^{3+} on the structural and magnetic properties of Cu nanosized ferrites for potential applications, Journal of Rare earths, 36 (2018) 156-164.
[24] K.K. Bharathi, C. Ramana, Improved electrical and dielectric properties of La-doped Co ferrite, Journal of Materials Research, 26 (2011) 584-591.
[25] P. Kumar, S. Sharma, M. Knobel, M. Singh, Effect of La^{3+} doping on the electric, dielectric and magnetic properties of cobalt ferrite processed by co-precipitation technique, Journal of Alloys Compounds, 508 (2010) 115-118.
[26] N. Hamdaoui, Y. Azizian-Kalandaragh, M. Khlifi, L. Beji, Cd-doping effect on morphologic, structural, magnetic and electrical properties of $Ni_{0.6-x}Cd_xMg_{0.4}Fe_2O_4$ spinel ferrite ($0\leq x\leq 0.4$), Journal of Alloys Compounds, 803 (2019) 964-970.
[27] M.M. Hossen, M.B. Hossen, Structural, electrical and magnetic properties of $Ni_{0.5}Cu_{0.2}Cd_{0.3}La_xFe_{2-x}O_4$ nano-ferrites due to lanthanum doping in the place of trivalent iron, Physica B: Condensed Matter, 585 (2020) 412116.
[28] S. Lorentzou, K. Karadimitra, C. Agrafiotis, A. Konstandopoulos, New routes for ferrite powders synthesis, in: PARTEC 2004, International Conference for Particle Technology, Nuremberg, Germany, Citeseer, 2004, pp. 16-18.
[29] E.C. Devi, P. Soibam, Effect of Zn doping on the structural, electrical and magnetic properties of $MnFe_2O_4$ nanoparticles, Indian Journal of Physics, 91 (2017) 861-867.
[30] S. Deepapriya, S.L. Devi, P.A. Vinosha, J.D. Rodney, C.J. Raj, J.E. Jose, Das, Estimating the ionicity of an inverse spinel ferrite and the cation distribution of La-doped $NiFe_2O_4$ nanocrystals for gas sensing properties, Applied Physics A, 125 (2019) 1-13.
[31] A. Aslam, A. Razzaq, S. Naz, N. Amin, M.I. Arshad, M.A.U. Nabi, A. Nawaz, K. Mahmood, A. Bibi, F. Iqbal, Impact of Lanthanum-Doping on the Physical and Electrical Properties of Cobalt Ferrites, Journal of Superconductivity and Novel Magnetism, (2021) 1-10.

[32] L. George, C. Viji, M. Maheen, E. Mohammed, Enhanced magnetic properties at low temperature of Mn substituted Ni-Zn mixed ferrite doped with Gd ions for magnetoresistive applications, Materials Research Bulletin, 126 (2020) 110833.
[33] K. Hussain, A. Bibi, F. Jabeen, N. Amin, K. Mahmood, A. Ali, M.Z. Iqbal, M. Arshad, Study of structural, optical, electrical and magnetic properties of Cu^{2+} doped $Zn_{0.4}Co_{0.6-x}Ce_{0.1}Fe_{1.9}O_4$ spinel ferrites, Physica B: Condensed Matter, 584 (2020) 412078.
[34] M.A.U. Nabi, M. Moin, M. Hasan, M. Arshad, A. Bibi, N. Amin, K. Mahmood, S. Ali, Study of Electrical Transport Properties of Cadmium-Doped Zn–Mn Soft Ferrites by Co-precipitation Method, Journal of Superconductivity and Novel Magnetism, (2020) 1-10.
[35] R. Kershi, Rare-earth ions as a key influencer on the magnetic, spectroscopic and elastic properties of $Er_\gamma Zn_{0.2}Co_{0.8}Fe_{2-\gamma}O_4$ nanoparticles, Journal of Alloys and Compound, (2020) 158114.
[36] B.P. Rao, B. Dhanalakshmi, S. Ramesh, P.M. Rao, M. Materials, Cation distribution of Ni-Zn-Mn ferrite nanoparticles, Journal of Magnetism and Magnetic Materials, 456 (2018) 444-450.
[37] C.A.P. Gómez, C.A.B. Meneses, S. Matute, Structural parameters and cation distributions in solid state synthesized Ni-Zn ferrites, Material Science and Engineering: B, 236 (2018) 48-55.
[38] I. Ahmad, T. Abbas, M. Islam, A. Maqsood, Study of cation distribution for Cu–Co nanoferrites synthesized by the sol–gel method, Ceramics International, 39 (2013) 6735-6741.
[39] S. Masoudpanah, S.S. Ebrahimi, M. Derakhshani, S. Mirkazemi, Structure and magnetic properties of La substituted ZnFe2O4 nanoparticles synthesized by sol–gel autocombustion method, Journal of magnetism and magnetic materials, 370 (2014) 122-126.
[40] E.E. Ateia, M. Ahmed, L. Salah, A. El-Gamal, Effect of rare earth oxides and La^{3+} ion concentration on some properties of Ni–Zn ferrites, Physica B: Condensed Matter, 445 (2014) 60-67.
[41] B.V. Prasad, B.R. Babu, M.S.R. Prasad, Structural and dielectric studies of Mg^{2+} substituted Ni–Zn ferrite, Materials Science-Poland, 33 (2015) 806-815.
[42] Q.-M. Wei, J.-B. Li, Y.-J. Chen, Cation distribution and infrared properties of $Ni_xMn_{1-x}Fe_2O_4$ ferrites, Journal of Materials Science, 36 (2001) 5115-5118.
[43] M.B. Mohamed, M. Yehia, Cation distribution and magnetic properties of nanocrystalline gallium substituted cobalt ferrite, Journal of Alloys and Compounds, 615 (2014) 181-187.
[44] K.A. Ganure, L.A. Dhale, S.E. Shirsat, K.S. Lohar, Morphological Study of Lanthanum-Doped Nano Spinel Ferrite via Normal Micelles Method, Journal of Inorganic and Organometallic Polymers and Materials, 28 (2018) 1821-1828.
[45] P. Thakur, R. Sharma, V. Sharma, P. Barman, M. Kumar, D. Barman, S. Katyal, P. Sharma, Gd^{3+} doped Mn-Zn soft ferrite nanoparticles: Superparamagnetism and its correlation with other physical properties, Journal of Magnetism and Magnetic Materials, 432 (2017) 208-217.
[46] J. Massoudi, M. Smari, K. Nouri, E. Dhahri, K. Khirouni, S. Bertaina, L. Bessais, Magnetic and spectroscopic properties of Ni–Zn–Al ferrite spinel: from the nanoscale to microscale, RSC Advances, 10 (2020) 34556-34580.
[47] G. Datt, M.S. Bishwas, M.M. Raja, A. Abhyankar, Observation of magnetic anomalies in one-step solvothermally synthesized nickel–cobalt ferrite nanoparticles, Nanoscale, 8 (2016) 5200-5213.
[48] M.I. Arshad, M. Hasan, A.U. Rehman, M. Akhtar, N. Amin, K. Mahmood, A. Ali, T. Trakoolwilaiwan, N.T.K. Thanh, Structural, optical, electrical, dielectric, molecular vibrational and magnetic properties of La^{3+} doped Mg–Cd–Cu ferrites prepared by Co-precipitation technique, Ceramics International, 48 (2022) 14246-14260.

[49] M. Raghasudha, D. Ravinder, P. Veerasomaiah, Electrical resistivity studies of Cr doped Mg nano-ferrites, Materials Discovery, 2 (2015) 50-54.
[50] S.B. Narang, K. Pubby, Nickel spinel ferrites: a review, Journal of Magnetism and Magnetic Materials, 519 (2021) 167163.
[51] M.Y. Lodhi, K. Mahmood, A. Mahmood, H. Malik, M.F. Warsi, I. Shakir, M. Asghar, M.A. Khan, New $Mg_{0.5}Co_xZn_{0.5-x}Fe_2O_4$ nano-ferrites: structural elucidation and electromagnetic behavior evaluation, Current Applied Physics, 14 (2014) 716-720.
[52] S.P. Dalawai, S. Kumar, M.A.S. Aly, M. Khan, H. Zaved, R. Xing, P.N. Vasambekar, S. Liu, A review of spinel-type of ferrite thick film technology: fabrication and application, Journal of Materials Science: Materials in Electronics, 30 (2019) 7752-7779.
[53] M. Arshad, S. Ikram, K. Mahmood, A. Ali, A. Nabi, N. Amin, F. Jabeen, Effect of la ions on nickel-cadmium spinel ferrites synthesized by co-precipitation method, Journal of Ovonic Research, 14 (2018) 27-34.
[54] A. Hao, X. Ning, Recent advances in spinel ferrite-based thin films: synthesis, performances, applications, and beyond, Frontiers in Materials, (2021) 501.
[55] H. Anwar, A. Maqsood, Enhancement of electrical and magnetic properties of Cd^{2+} doped Mn–Zn soft nanoferrites prepared by the sol–gel autocombustion method, Journal of magnetism and magnetic materials, 333 (2013) 46-52.
[56] M. Eltabey, A. Massoud, C. Radu, Microstructure and superparamagnetic properties of Mg-Ni-Cd ferrites nanoparticles, Journal of Nanomaterials, 2014 (2014) 492832.
[57] C. Y. Tsay, Y. C. Chiu, C. M. Lei, Hydrothermally synthesized Mg-based spinel nanoferrites: Phase formation and study on magnetic features and microwave characteristics, Materials, 11 (2018) 2274.
[58] A. Majeed, M.A. Khan, F. ur Raheem, A. Hussain, F. Iqbal, G. Murtaza, M.N. Akhtar, I. Shakir, M.F. Warsi, Structural elucidation and magnetic behavior evaluation of rare earth (La, Nd, Gd, Tb, Dy) doped BaCoNi-X hexagonal nano-sized ferrites, Journal of magnetism and magnetic materials, 408 (2016) 147-151.
[59] S. Gaba, A. Kumar, P.S. Rana, M. Arora, Influence of La^{3+} ion doping on physical properties of magnesium nanoferrites for microwave absorption application, Journal of Magnetism and Magnetic Materials, 460 (2018) 69-77.
[60] A.U. Rehman, N. Amin, M.B. Tahir, M.A. un Nabi, N. Morley, M. Alzaid, M. Amami, M. Akhtar, M.I. Arshad, Evaluation of spectral, optoelectrical, dielectric, magnetic, and morphological properties of RE^{3+} (La^{3+}, and Ce^{3+}) and Co^{2+} co-doped $Zn_{0.75}Cu_{0.25}Fe_2O_4$ ferrites, Materials Chemistry and Physics, 275 (2022) 125301.